

Optical phased arrays for LIDAR: beam steering via tunable plasmonic metasurfaces

Antonino Calà Lesina^{1,2,3,*}, Dominic Goodwill⁴, Eric Bernier⁴, Lora Ramunno^{1,2}, and Pierre Berini^{1,2,3}

¹Department of Physics, University of Ottawa, Ottawa, Canada.

²Centre for Research in Photonics, University of Ottawa, Ottawa, Canada.

³School of Electrical Engineering and Computer Science, University of Ottawa, Ottawa, Canada.

⁴Huawei Technologies Canada, Ottawa, Canada.

*antonino.calalesina@uottawa.ca

Abstract

Controlling the phase and amplitude of light emitted by the elements (*i.e.*, pixels) of an optical phased array is of paramount importance to realizing dynamic beam steering for LIDAR applications. In this paper, we propose a plasmonic pixel composed of a metallic nanoantenna covered by a thin oxide layer, and a conductive oxide, *e.g.*, ITO, for use in a reflectarray metasurface. By considering voltage biasing of the nanoantenna via metallic connectors, and exploiting the carrier refraction effect in the metal-oxide-semiconductor capacitor in the accumulation and depletion regions, our simulations predict control of the reflection coefficient phase over a range $> 330^\circ$ with a nearly constant magnitude. We discuss the physical mechanism underlying the optical response, the effect of the connectors, and propose strategies to maximize the magnitude of the reflection coefficient and to achieve dual-band operation. The suitability of our plasmonic pixel design for beam steering in LIDAR is demonstrated via 3D-FDTD simulations.

1 Introduction

Most commercial light detection and ranging (LIDAR) scanners are too bulky and slow for applications requiring a high refresh rate, such as self-driving cars and autonomous machines. Optical phased arrays [1] are much smaller and can tremendously improve the scanning speed as they rely on electronic steering rather than mechanical. An optical phased array is composed of phase-tunable light emitters spatially arranged on a plane, where a single emitter is referred to as a pixel. A pixel can be a source of light, such as a LASER, a waveguide, or a LED. However, a pixel can also be a scatterer, such as a nanostructure in a reflectarray or transmitarray metasurface.

Beam steering via optical phased array is achieved by imposing a phase gradient along a certain direction in the array. Extraneous beams, *e.g.*, produced by grating lobes, need to be minimized in LIDAR applications as they can produce false positives during the scanning process. The pitch a of a matrix of pixels (*i.e.*, the spacing between emitters) if too large, can cause grating lobes of similar amplitude as the main lobe. In order to avoid these grating lobes for any steering angle, the pitch should satisfy $a < \lambda/2$, where λ is the wavelength in the material in which the array is immersed. This requirement trades off with the necessity of having a large enough pitch so that pixels do not interact with each other (no near-field coupling), and each can be controlled independently. Furthermore, if the phase of the field emitted by the pixel does not cover a 360° range, or its amplitude is not uniform across the phase range, the phase gradient will contain imperfections. These imperfections can be periodic with a period much greater than the pitch, thus producing lobes obeying a diffraction grating-type equation; we call these “long-period grating lobes”.

Among phase-shifting pixels for optical phased arrays, those based on plasmonic resonances can satisfy $a < \lambda/2$. Thus, plasmonic metasurfaces [2–5] offer a platform to implement optical phased arrays that completely avoid grating lobes arising from a too large pitch size. Most plasmonic metasurfaces experimentally demonstrated to date are passive; this means that once fabricated, they cannot be further tuned resulting in a static optical response. Such passive metasurfaces have been proposed for focusing [6], achromatic lensing [7], perfect absorption [8], colouring [9], performing mathematical operations [10], holography [11], nonlinear field enhancement [12], beam structuring in the linear [13] and nonlinear [14] regimes, and biosensing [15]. However, there is a growing interest in active plasmonics to control the field emitted by individual nanostructures by tuning their surface plasmon resonances [16], and in tunable metasurfaces with reconfigurable optical response [17, 18] for applications in dynamic holography and optical information encryption [19], adaptive beamforming in wireless communications [20], chirality switching [21], active displays [22], polarization conversion [23], metalenses with tunable focus [24], dynamic beam steering [25, 26], and intensity modulators [27].

A pixel controllable in phase can be achieved by exploiting, for example, phase-change materials [28], liquid crystals [29], Fermi-level gating in graphene [30], carrier refraction in semiconductors and transparent conductive oxides (TCOs) including indium-tin oxide (ITO) [31, 32], and the thermo-optic effect in bulk dielectrics [33]. Phase control has also been demonstrated in arrays of coherently-coupled vertical-cavity surface-emitting lasers [34], and via voltage-tunable inter-subband transitions in semiconductor heterostructures exploiting the quantum-confined Stark effect [35].

Tuning the response of plasmonic nanostructures by exploiting the carrier refraction effect in ITO is promising because of the large change in refractive index available in this material (of the order of unity) [36, 37]. Recent experimental [31, 32] and theoretical [26, 38] studies of phase control for beam steering and focusing, using metallic or dielectric resonant systems, are encouraging. In [31, 32, 38], out-of-plane field enhancement was exploited in metal-insulator-metal (MIM) nano-resonators, where oxide and ITO were placed between the two metal layers. In these cases, the carrier density variation was induced in ITO via single [31] or double [32] gating. The bottom layer was a plane metallic surface, whereas the other layer was either a linear [31, 38] or fishbone [32] grating. The phase range achieved in MIM configurations was $< 300^\circ$ [26, 38] for single gating. To achieve a phase range $> 300^\circ$ a dual-gated solution was proposed [32].

Here we propose a plasmonic pixel for phase control which can be used in a reflectarray metasurface for optical beam steering. The pixel is composed of a metallic dipole nanoantenna covered by oxide and ITO. We exploit the perturbation of the permittivity of ITO at locations where the nanostructure creates strong field enhancement in the direction of the nanoantenna axis rather than in the out-of-plane direction as in MIM structures, that is, at the nanoantenna extremities and within its gap. Exploiting the field enhancement in the gap of a dipole nanoantenna to control the phase of its reflection coefficient has yet to be reported - we show how this plays a major role in achieving reflection with a large tunable phase and an approximately constant magnitude of the reflection coefficient.

The permittivity of ITO is perturbed via the carrier refraction effect induced in the material, as ITO operates electrically as the semiconductor in a MOS capacitor. In particular, through voltage gating enabled by metallic connectors, we induce a perturbation of the carrier density over a thin ITO region near the nanoantenna via accumulation and depletion processes. In accumulation, the carrier density increases, producing a blue-shift of the epsilon-near-zero wavelength, λ_{ENZ} , of the ITO in this thin perturbed region. As the carrier density increases further, λ_{ENZ} eventually passes through the resonance wavelength of the nanoantenna, and the system transitions from a nanoantenna immersed in a dielectric to a nanoantenna surrounded by a metallic shell. This produces a large red-shift of the nanoantenna resonance wavelength, and as we show in detail, is responsible for the large phase variation observed. We also demonstrate that the phase range can be extended by driving the MOS capacitor into depletion, as depleting the carrier density over an increasing thickness produces an additional sizable phase shift.

Our proposed pixel satisfies the conditions discussed above to minimize grating lobes in optical beam steering, as we will show in Section 2 via detailed optical and electrostatic simulations. After presenting the numerical approach (2.1) and an optimized pixel design via detailed optical simulation (2.2), we explain the physical mechanism underlying the large phase shift (2.3), and propose a strategy for increasing the amplitude and uniformity of the reflection amplitude (2.4). We then explore the effect of the metallic connector position on the resonance of the nanoantenna, and show how this can be exploited to design a dual-band pixel at telecom wavelengths (2.5). Our ITO perturbation model is justified via detailed electrostatic simulations (2.6). Finally, the use of our proposed pixel for beam steering is demonstrated in Section 3 via 3D simulations of an array using the finite-difference time-domain method (FDTD).

2 Plasmonic pixel design

2.1 Optical simulation approach

2.1.1 Description of the pixel

In Fig. 1(a), we show a sketch of a metasurface that uses, as a building block, our proposed plasmonic pixel illustrated in top-view in Fig. 1(b). The pixel has dimensions a_x by a_z , and contains a gold dipole nanoantenna, which is formed by two branches of length L_d , width w , thickness t , separated by a gap of size g . The pixel also contains two gold lines of width w_c , perpendicular to the dipole, which serve as electrical connectors; the distance between the edge of the connector and the edge of the nanoantenna gap is denoted by p_c . Here, the connectors are placed in the centre of the branches, so that $p_c = 0.5 \cdot (L_d - w_c)$, but they can be located at an arbitrary distance p_c from the edge of the nanoantenna gaps.

The nanoantenna of thickness t sits on a glass substrate, and the nanoantenna/glass system is covered conformally by a thin oxide (hafnia) layer of thickness t_{ox} , which is then covered by ITO; see the side view of the pixel illustrated in Fig. 1(c). We denote the thickness of the metasurface (metal nanostructure+oxide+ITO) by t_m . A gold backplane is placed on top of the ITO allowing us to use the pixel in reflection through the glass substrate. The backplane is depicted here as a flat layer on planarized ITO but it could also be conformal. The electrically-contacted nanoantennas form the metallization of the MOS capacitor and the gold backplane its ground, with the oxide and ITO forming the insulator and semiconductor regions, respectively. In Figs. 1(b) and 1(c), we also indicate by the red dashed line the thin ITO layer of thickness t_{pert} , whose refractive index is perturbed by the carrier refraction effect in the MOS capacitor. All corners in

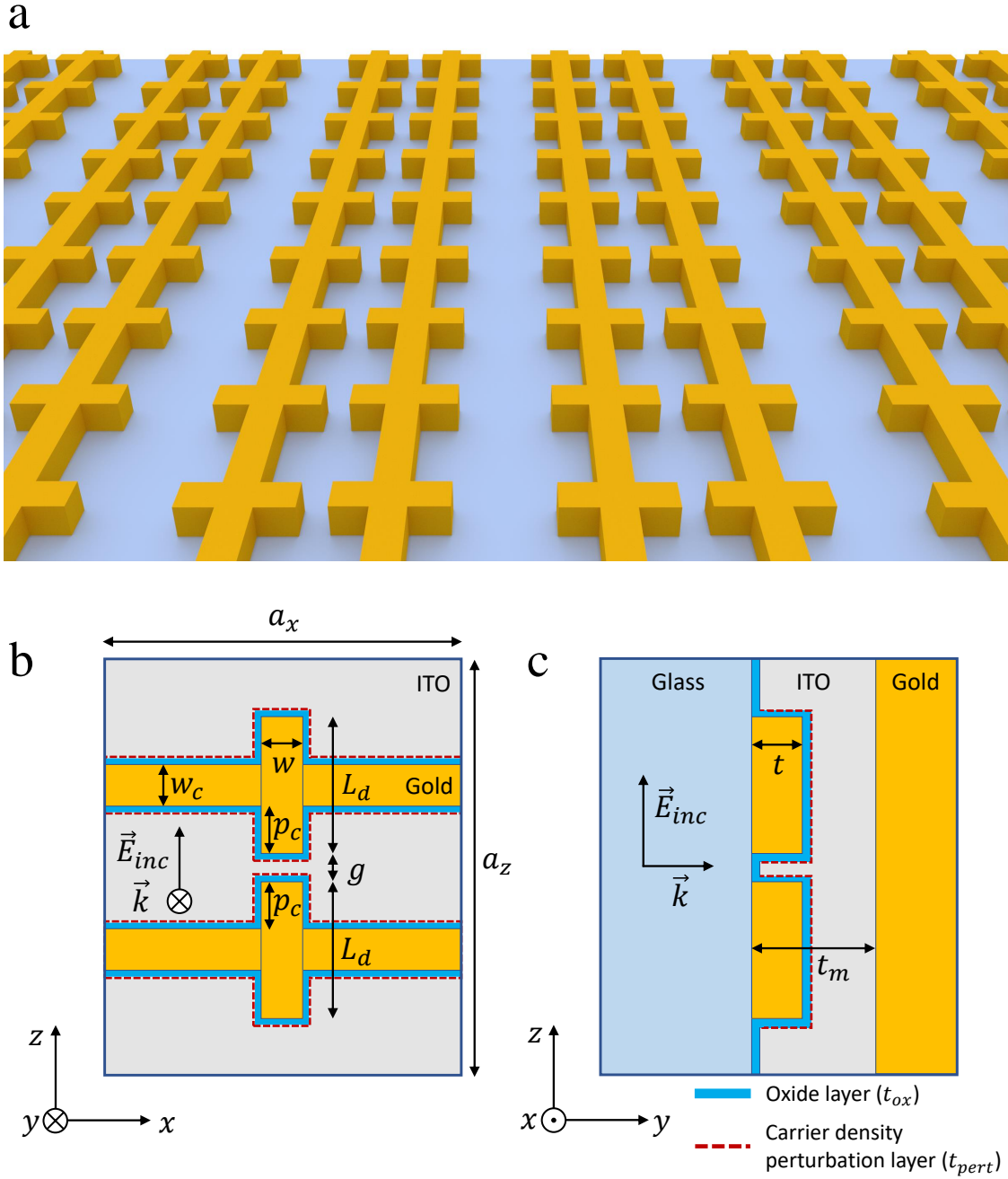


Figure 1: (a) Metasurface containing an array of plasmonic pixels (only glass substrate and gold nanoantennas are sketched). (b) Top view, and (c) cross-sectional view of the proposed plasmonic pixel. Throughout this paper, several parameters will remain fixed at the following optimized values: $a_z = 500$ nm, $w = 50$ nm, $w_c = 50$ nm, $t = 50$ nm, and $t_{ox} = 5$ nm.

our optical computations are square for ease of simulation, as we find that the optical response is not significantly altered by using rounded corners.

2.1.2 Simulation details

The optical modelling was conducted with in-house 3D FDTD software [39,40]. Based on fabrication constraints and optical performance evaluated via detailed numerical simulations, we found optimal values for a_z , w , w_c , t , and t_{ox} (see the caption of Fig. 1), and they will not be varied throughout this paper. We consider optical (vacuum) wavelengths in the range $\lambda_0 = 1000$ to 1800 nm due to the availability of high-performance, compact and inexpensive laser sources in that range, and all our designs are optimized to operate at telecom wavelengths, *e.g.*, $\lambda_0 = 1550$ nm.

Gold is modelled using the complex permittivity from [41] via the Drude model, *i.e.*, $\varepsilon_r(\omega) = \varepsilon_\infty - \frac{\omega_p^2}{\omega^2 + i\gamma\omega}$, where $\varepsilon_\infty = 8.4156$, $\gamma = 4.8257 \cdot 10^{13}$ rad/s, and $\omega_p = 1.4117 \cdot 10^{16}$ rad/s. We choose hafnia (HfO₂) as our insulator, with a layer thickness $t_{ox} = 5$ nm; it is modelled as a lossless and dispersionless dielectric of refractive index $n_{ox} = 2.0709$ [42] (sampled at $\lambda_c = 1550$ nm). Glass is simulated as a dispersionless material with $n_{SiO_2} = 1.45$. The permittivity of ITO is modelled via the Drude model with $\varepsilon_\infty = 4.2345$, $\gamma = 1.7588 \cdot 10^{14}$ rad/s, and an ω_p that varies with carrier density N according to $\omega_p = \sqrt{Ne^2/(\varepsilon_0 m_n^*)}$, where e is the electron charge, ε_0 the vacuum permittivity, and $m_n^* = 0.35 \cdot m_e$ the effective mass of electrons; m_e is the free electron mass. The unperturbed carrier density of ITO is taken as $N_0 = 3 \cdot 10^{20}$ cm⁻³, which corresponds to a plasma frequency $\omega_p = 1.652 \cdot 10^{15}$ rad/s [31,32].

To optimize the design, we consider an infinite 2D array of the plasmonic pixel, though we simulate only a single unit cell containing one pixel. The unit cell is excited with a z -polarized broadband plane wave pulse propagating along y , and periodic boundary conditions are applied along x and z . We discretize all space dimensions with a uniform space step of 1 nm [40]. We calculate the reflection coefficient $\Gamma(\omega) = E_z(\omega)/E_{inc}(\omega)$, from the known incident field $E_{inc}(\omega)$ and reflected field $E_z(\omega)$; the latter is the only nonzero far-field component due to the z -polarized applied excitation. The reflected field is obtained in the scattered field region at a distance of 600 nm from the nanoantenna, which can be considered far-field for plasmonic systems. At this distance, the reflected field is a plane wave due to the sub-wavelength pixel size and consequent lack of diffraction orders (a_x and $a_z < \lambda/2$, where $\lambda = \lambda_0/n_{SiO_2}$, and λ_0 is the vacuum wavelength). The reflectance is defined as $|\Gamma|^2$ and represents the attenuation factor applicable to the optical power.

2.1.3 Carrier refraction effect

From the Drude model introduced above, we note that the plasma frequency scales with \sqrt{N} : this is the origin of the carrier refraction effect. The carrier density can be varied within a thin layer of ITO by exploiting the operation of a MOS capacitor, where the metal nanoantenna represents the gate (connected to a voltage V_g), ITO is used as the semiconductor (connected to a voltage $V_s = 0$ V or ground), and a thin insulating (oxide) layer is placed in between. We consider both connectors of the pixel pinned to the same potential (symmetric perturbation), but dual-gating can also be exploited. As explored in more detail via electrostatic simulations in subsection 2.6, when a voltage bias V_g is applied to the gate relative to ground, the carrier density changes within a thin ITO layer due to accumulation ($V_g > V_{fb}$) or depletion ($V_g < V_{fb}$) processes, where V_{fb} is the flat band voltage of our MOS capacitor. This local change in carrier density produces a local change in permittivity due to the carrier refraction effect. Since the ITO layer with perturbed carrier density is located in the enhanced field region near the plasmonic nanostructure, its refractive index variation modifies the resonance condition of the nanoantenna and, therewith, the phase of the reflected field.

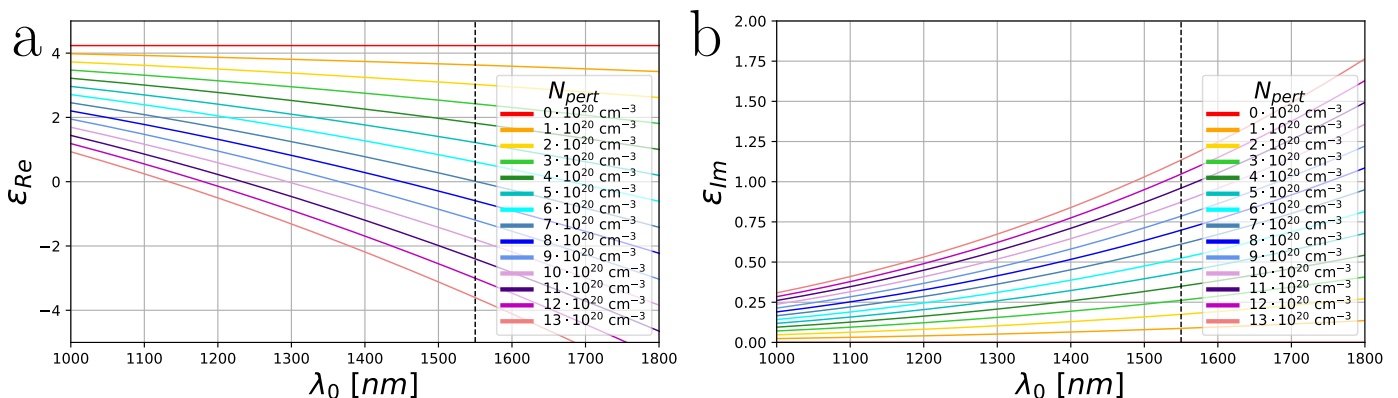


Figure 2: (a) ε_{Re} and (b) ε_{Im} of ITO *vs.* λ_0 for varying N_{pert} . This permittivity is applied within the perturbed ITO layer of thickness t_{pert} in the optical model.

Based on the electrostatic analysis of the MOS capacitor in subsection 2.6, we model the local carrier refraction effect in ITO by introducing in the optical model a thin layer of ITO with thickness $t_{pert} = 1$ nm, as shown in Figs. 1(b) and (c). The carrier density within the t_{pert} layer is considered uniform and denoted by N_{pert} . The permittivity of the t_{pert} layer is shown in Fig. 2, and we see that the epsilon near zero wavelength λ_{ENZ} – that is, the wavelength for which $\epsilon_{Re} = 0$ – blue shifts with increasing N_{pert} . Here N_{pert} is allowed to range between 0 and N_0 in depletion, and N_0 and $13 \cdot 10^{20} \text{ cm}^{-3}$ in accumulation, for a V_g constrained within the breakdown voltage limits, *i.e.*, $|V_g| < V_{bk} = 3.2$ V. Under negative bias, as we will show in subsection 2.6, the width of the depletion region increases up to $t_{pert} = 2$ nm for $V_g = -V_{bk}$, and this case is considered in optical simulations as well.

2.2 Optical performance of plasmonic pixel

Now that we have introduced the concept of our plasmonic pixel and how it operates, we turn to the calculation of the reflection coefficient and how it changes as a function of N_{pert} (and thus, gate voltage) in the perturbed ITO layer. We show in Fig. 3 the results for an optimized pixel (with dimensions as reported in the figure caption). In Fig. 3(a), we plot the absolute value of the reflection coefficient $|\Gamma|$ as a function of λ_0 and N_{pert} (15 simulation entries). The most obvious and remarkable feature of Fig. 3(a) is that there is a wavelength – called the constant amplitude wavelength, λ_c – for which $|\Gamma|$ has approximately the same value for all values of N_{pert} – we call this the constant amplitude point, corresponding to a set of 15 reflection coefficient amplitudes, that are almost coincident. The optimization of the pixel is conducted such that λ_c coincides with the operating wavelength, *i.e.*, $\lambda_c = 1550$ nm (vertical black dashed line). Furthermore, plotting the phase of Γ ($\angle \Gamma$) in Fig. 3(b), we see that at λ_c (vertical black dashed line) there is a large variation with N_{pert} .

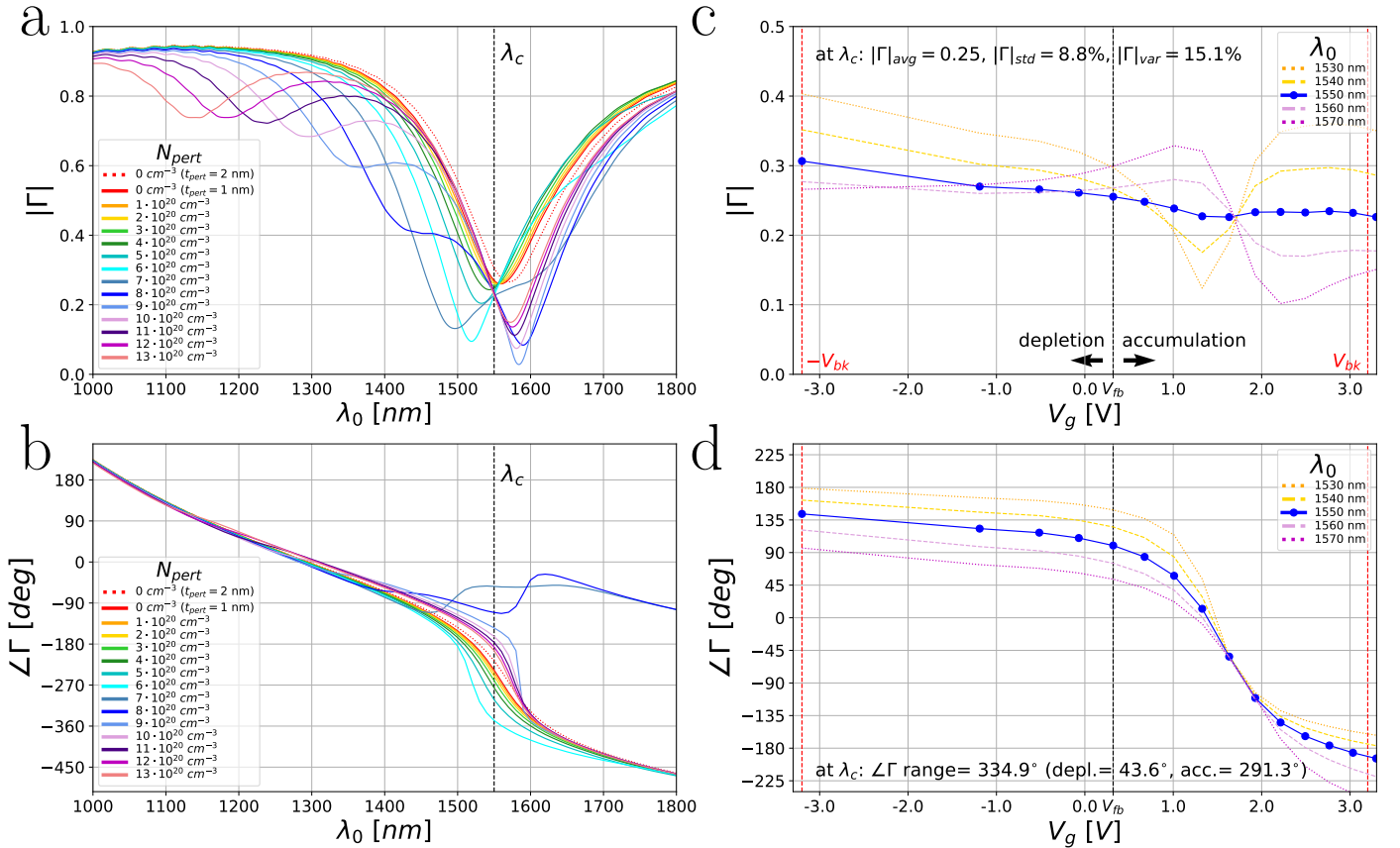


Figure 3: An optimized pixel with parameters $g = 30$ nm, $L_d = 194$ nm, $a_x = 500$ nm, $t_m = 89$ nm, and $p_c = 0.4 \cdot (L_d - w_c)$: (a) $|\Gamma|$ and (b) $\angle \Gamma$ vs λ_0 for varying N_{pert} within the t_{pert} layer. (c) $|\Gamma|$ and (d) $\angle \Gamma$ vs V_g for λ_0 near λ_c . The phase plots are unwrapped for clarity.

Using the relation between V_g and N_{pert} obtained by electrostatic simulations in subsection 2.6, we plot $|\Gamma|$ and $\angle \Gamma$ in Figs. 3(c) and 3(d), respectively, as functions of V_g for wavelengths close to λ_c . Here it is evident that at λ_c , $|\Gamma|$ is nearly constant and $\angle \Gamma$ goes through a large variation. These are desirable characteristics for the realization of beam steering at λ_c with long-period grating lobes within an acceptable level. Considering all the 15 simulation entries (highlighted as blue dots in Fig. 3(c)) from Fig. 3(a) at λ_c , we obtain an average reflection coefficient $|\Gamma|_{avg} \sim 0.25$. Not only should $|\Gamma|_{avg}$ be large, but the sequence of blue dots in Fig. 3(c) should also be flat. This means that the percentage standard

deviation and the percentage variation of $|\Gamma|$, indicated as $|\Gamma|_{std}$ and $|\Gamma|_{var} = \frac{|\Gamma|_{max} - |\Gamma|_{min}}{|\Gamma|_{max} + |\Gamma|_{min}}$, respectively, and reported in Fig. 3(c), have to be as small as possible, ideally zero, in order to reduce the level of the long-period grating lobes of a steered beam.

As reported in Fig. 3(d), the phase range achieved at λ_c within the voltage breakdown limit is $\sim 334^\circ$, where $\sim 291^\circ$ is obtained in accumulation and $\sim 43^\circ$ in depletion. In accumulation, λ_{ENZ} of the perturbed ITO layer passes through λ_c as N_{pert} increases; this is evident in Fig. 3(a), where the $|\Gamma|$ curves show a resonance dip close to λ_{ENZ} which blue-shifts for increasing N_{pert} . This mechanism plays the main role in shifting the phase of the reflection coefficient, as we explain in more detail in subsection 2.3. As already mentioned, we also consider the case $N_{pert} = 0 \text{ cm}^{-3}$ with $t_{pert} = 2 \text{ nm}$, which can be reached by the MOS capacitor in depletion at the limit of the oxide breakdown. This simulation condition is reported in Fig. 3(a) as the red dotted curve, and shows a red shift of the response with respect to λ_c . The red shift is due to the larger t_{pert} , and results in an increase in $|\Gamma|$ in Fig. 3(c) as V_g approaches $-V_{bk} = -3.2 \text{ V}$.

2.3 Effect on phase shift due to changing λ_{ENZ}

To better understand the operation of our plasmonic pixel and see more clearly how the resonance dips evolve with increasing N_{pert} , we plot in Fig. 4(a) the spectra from Fig. 3(a), but spread out along the horizontal axis. The operating wavelength $\lambda_c = 1550 \text{ nm}$ is indicated by the vertical black dashed line. As we can see, this wavelength coincides with the resonance dip of the system in the unperturbed case ($N_{pert} = 3 \cdot 10^{20} \text{ cm}^{-3}$). The red dotted curve in Fig. 4(a) tracks the value λ_{ENZ} within the perturbed ITO layer as N_{pert} is varied, which we can see is associated with a closely located resonance dip. The green dashed line tracks the evolution of the main nanoantenna resonance dip.

When $\lambda_{ENZ} > \lambda_c$, the perturbed ITO layer around the nanoantenna is dielectric and its refractive index decreases with increasing N_{pert} , producing a blue shift of the main nanoantenna resonance dip (see green dashed line for $N_{pert} \leq 7 \cdot 10^{20} \text{ cm}^{-3}$). This suddenly changes when λ_{ENZ} passes through λ_c (see intersection of red dotted curve and black dashed line). For $\lambda_{ENZ} < \lambda_c$, the perturbed ITO layer becomes a metallic sheath, which makes the nanoantenna effectively larger and produces a sudden red-shift of the resonance wavelength (see jump of the green dashed line for $N_{pert} > 7 \cdot 10^{20} \text{ cm}^{-3}$).

We need to point out that this phase shift mechanism can only work if λ_{ENZ} for the unperturbed ITO is greater than the resonance wavelength of the nanoantenna. This condition can be satisfied in ITO and other TCO materials, where the free carrier density can be regulated so that λ_{ENZ} is located in the infrared.

In Fig. 4(b), we plot the field distributions associated with the dips labelled by the encircled numerals in Fig. 4(a). We observe the evolution of the resonance mode (tracked by the green dashed line in Fig. 4(a)), and find that it corresponds to a notable field enhancement in the gap of the dipole nanoantenna. This mode evolves following the field distributions labelled by 1-2-5-7-9 in Fig. 4(b) and this series contains the λ_{ENZ} jump across λ_c . The mode associated with the evolution of λ_{ENZ} , indicated by the red dotted curve in Fig. 4(a), follows the field distributions labelled by 3-4-6-8 in Fig. 4(b). This mode is characterized by field enhancement in the thin perturbed ITO layer, as is particularly evident in field distributions 4, 6 and 8 of Fig. 4(b). We notice that for $N_{pert} = 7 \cdot 10^{20} \text{ cm}^{-3}$, $\lambda_{ENZ} \sim \lambda_c$, the resonance mode of the nanostructure is hybridized, and the field distributions labelled 2 and 3 in Fig. 4(b) are similar.

2.4 Optimizing the reflection coefficient amplitude and uniformity

In this subsection we describe strategies for increasing the reflectance at λ_c in the interests of increasing the power efficiency in beam steering applications, and making the reflectance as uniform as possible with varying V_g . To increase pixel reflectance, we increase the field enhancement in the gap of the dipole nanoantenna by reducing the gap length. As the gap must contain two oxide layers, this sets a limit on the smallest possible gap. In Fig. 5, we report the optical simulation results for a second pixel optimized to exhibit a constant amplitude point at λ_c . In this case, the average reflection coefficient at λ_c is 0.4 – two times higher than our previous design above – which yields a $\sim 20\%$ reflectance; the percentage variation is $\sim 11\%$. The phase range in depletion is $\sim 64^\circ$, which is higher than what was reported in Fig. 3 due to the fact that for $t_{pert} = 2 \text{ nm}$, the gap is almost completely depleted. However, the overall phase range ($\sim 305^\circ$) is lower than that reported in Fig. 3, which suggests that the phase range trades-off against reflectance.

In Fig. 6, we show the optical simulation results for a third pixel optimized to exhibit a constant amplitude point at λ_c . As an appendix to Fig. 6, we show in File 1 (Supporting Information) how the variation of the geometric parameters a_x , t , t_m , and w affects the amplitude of the resonance dips of the $|\Gamma|$ curves (*i.e.*, they move up and down), but with a negligible spectral shift. This affects the intersection of the curves and in turn the uniformity of the reflection coefficient at λ_c . In particular, we observe that decreasing a_x , or increasing t , t_m , or w contribute to the formation of the constant amplitude point in a qualitatively similar way. Furthermore, by comparing Fig. 6 to Fig. 3, we note that in Fig. 6 we have slightly lower $|\Gamma|_{avg}$ and phase range, though $g = 30 \text{ nm}$ in both cases. This suggests that merging the two resonances of the system, as was the case for the optimized design in Fig. 3, may provide a strategy to improve reflectance and phase range. This merging can be achieved by optimizing the connector position, to which we now turn.

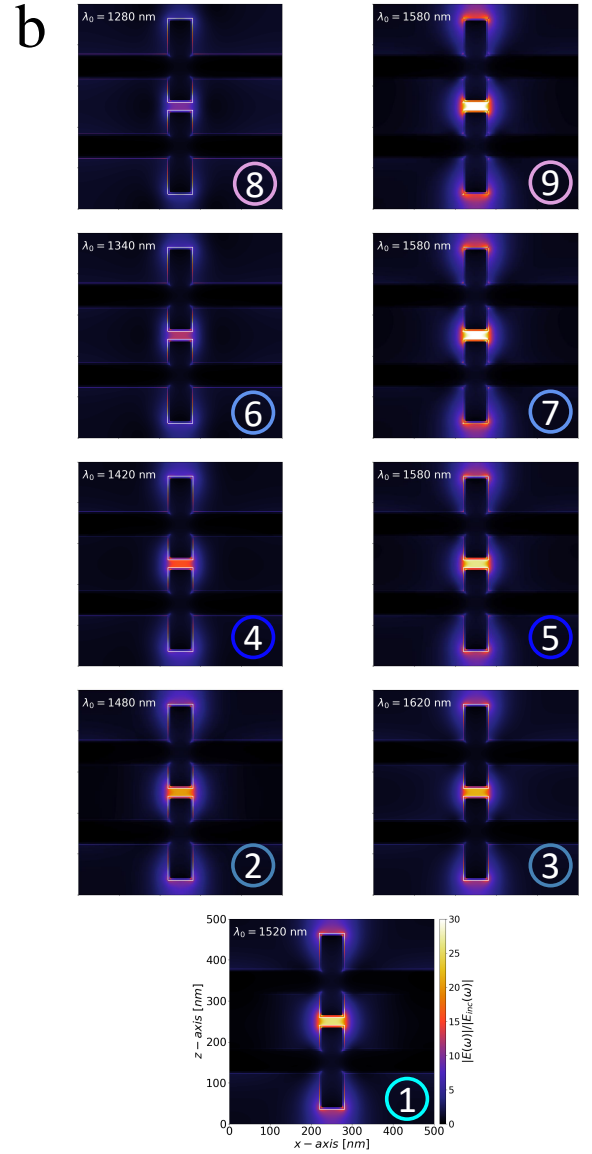
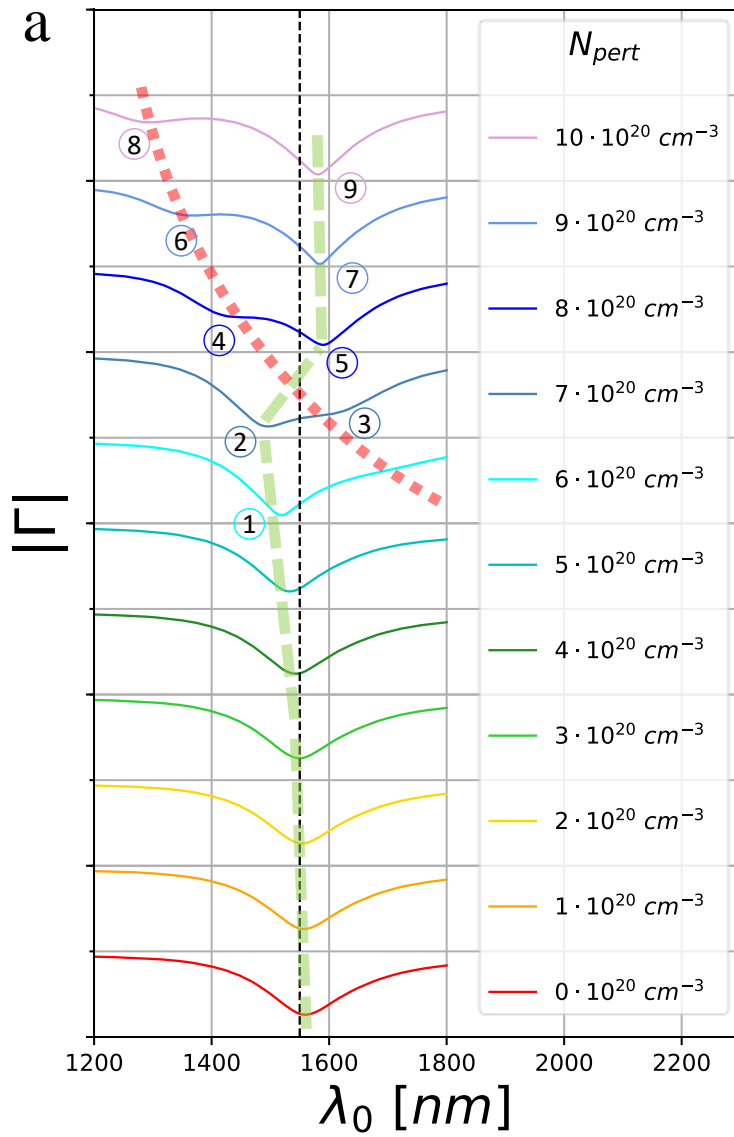


Figure 4: Response of the optimized pixel of Fig. 3: (a) $|\Gamma|$ vs λ_0 for varying N_{pert} as indicated in the legend. (b) Field distribution within the pixel for wavelengths corresponding to the resonances identified by numerals in Fig. 4(a).

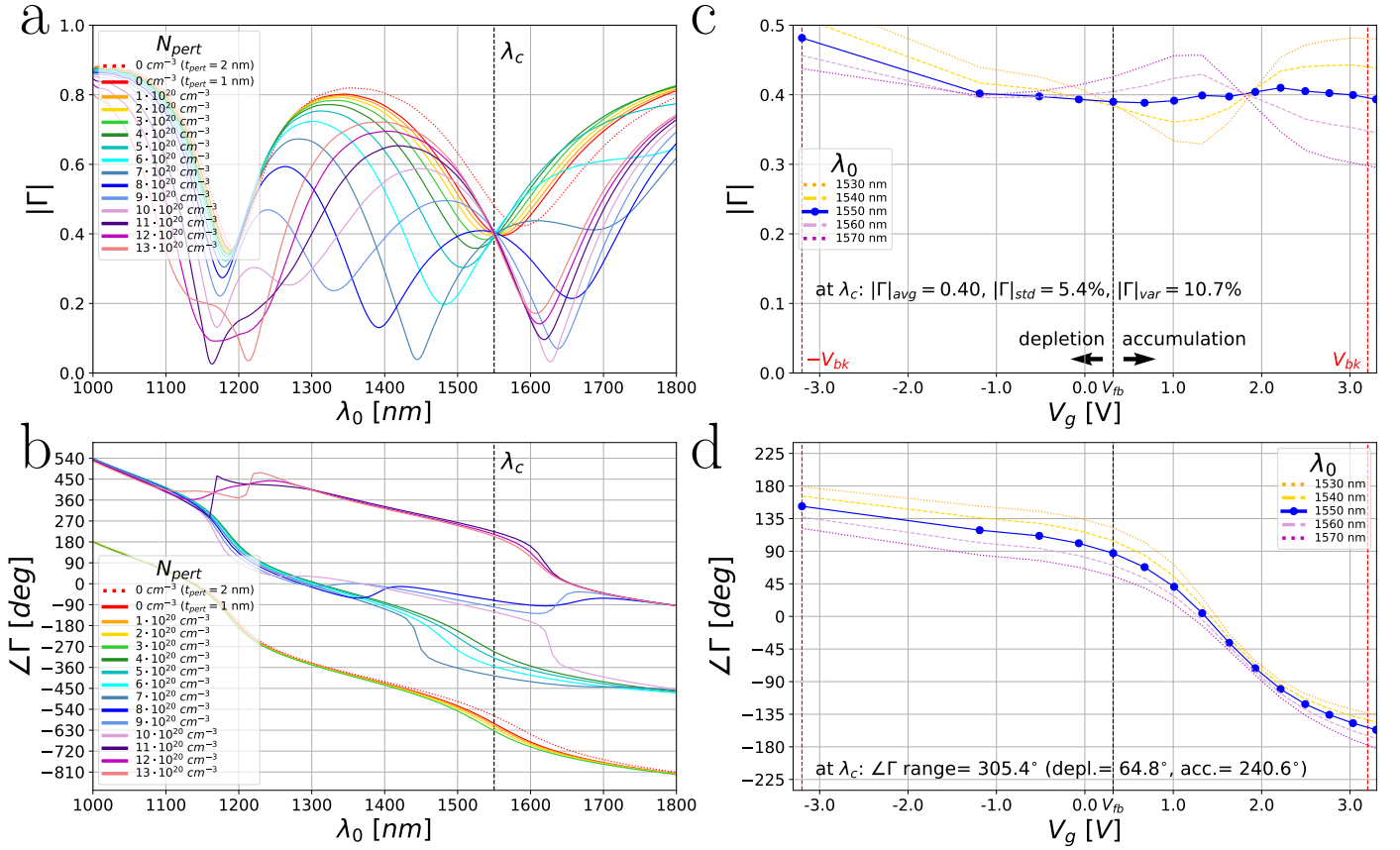


Figure 5: Second optimized pixel with parameters $g = 15 \text{ nm}$, $L_d = 149 \text{ nm}$, $a_x = 298 \text{ nm}$, $t_m = 100 \text{ nm}$, and $p_c = 0.5 \cdot (L_d - w_c)$: (a) $|\Gamma|$ and (b) $\angle \Gamma$ vs λ_0 for varying N_{pert} within the t_{pert} layer. (c) $|\Gamma|$ and (d) $\angle \Gamma$ vs V_g for λ_0 near λ_c . The phase plots are unwrapped for clarity.

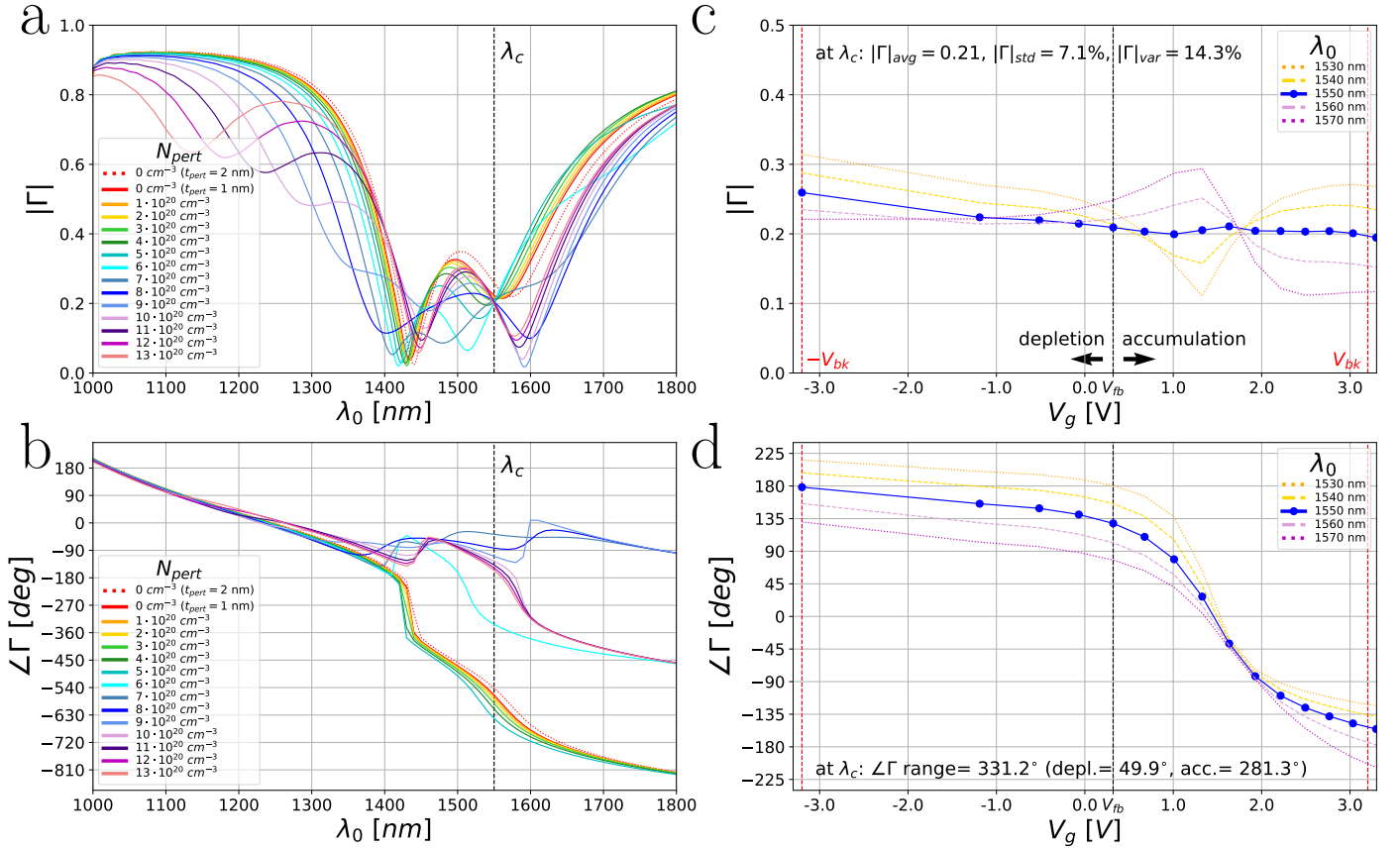


Figure 6: Third optimized pixel with parameters $g = 30 \text{ nm}$, $L_d = 186 \text{ nm}$, $a_x = 404 \text{ nm}$, $t_m = 100 \text{ nm}$, and $p_c = 0.5 \cdot (L_d - w_c)$: (a) $|\Gamma|$ and (b) $\angle \Gamma$ vs λ_0 for varying N_{pert} within the t_{pert} layer. (c) $|\Gamma|$ and (d) $\angle \Gamma$ vs V_g for λ_0 near λ_c . The phase plots are unwrapped for clarity.

2.5 Effect of the connector position and dual-band pixel

We demonstrate in this subsection that the position of the connectors in the pixel significantly alters the optical response. This is an important aspect for the experimental realization of this type of structure. Here we consider only the case where the two sets of connectors are equally distant from the gap, *i.e.*, we use the same value of p_c for both branches of the dipole nanoantenna. For the optimized pixel reported in Fig. 3, we used $p_c = 0.4 \cdot (L_d - w_c)$, which results in the plasmonic system exhibiting only one resonance, rendering the connectors optically non-invasive. In the optimized pixels in subsection 2.4, we used $p_c = 0.5 \cdot (L_d - w_c)$, and this resulted in the reflection coefficient amplitude curves each exhibiting two resonances. Using the parameters of the pixel in Fig. 6 but considering different connector positions, p_c , we will explore the effect of the connector location on the optical response, and the origin of these two resonances.

Considering here unperturbed ITO ($N_{pert} = N_0$), we varied the connector position from $p_c = 0$ to $p_c = L_d - w_c$ to investigate how the resonances evolve with changing p_c . In Fig. 7(a), from bottom to top, we sketch a dipole nanoantenna without connectors, with connectors at position $p_c = 0$ (*i.e.*, located on either side of the gap), with connectors at position $p_c = 0.5 \cdot (L_d - w_c)$ (middle of the branches), and with connectors at position $p_c = L_d - w_c$ (at the extremities of the dipole nanoantenna). In Fig. 7(b), we show the evolution of $|\Gamma|$ as a function of p_c . For some of the resonances in the reflection coefficient, identified by numerals in Fig. 7(b), we plot the corresponding magnitude of the electric near-field in Fig. 7(c). We observe that the single resonance in the case with no connectors splits into two when connectors are introduced: the primary resonance produces field enhancement in the gap of the nanoantenna, whereas the secondary resonance produces field enhancement at the extremities of the branches of the dipole nanoantenna. In the no connector case (field distribution 1, bottom), field enhancement exists in both the gap and the branch extremities. As p_c increases, the two resonances evolve in the spectrum tracing out an “X”, *i.e.*, as the primary resonance red-shifts and the secondary resonance blue-shifts (see grey dashed line and grey solid line in Fig. 7(b), respectively). There is a connector position for which the two resonances overlap, which for our example is at $p_c = 0.4 \cdot (L_d - w_c)$ (field distribution identified by numeral 6). This mode strongly resembles the no connector case and identifies the position selected in order for the effect of the connectors on the resonance of the nanoantenna to be minimized. This is the connector position used in our optimized pixel in Fig. 3.

However, the two resonances obtained by introducing the connectors can also be exploited. In Fig. 8, we show results for a fourth optimized pixel that can be used for dual-band beam steering, as it exhibits two constant amplitude wavelengths at the telecom wavelengths $\lambda_c = 1550$ nm and $\lambda_c^{(2)} = 1310$ nm. The phase shifting at both operating wavelengths occurs as λ_{ENZ} transitions through the resonance wavelengths. At λ_c , we have the primary resonance with field enhancement in the gap. In this case, $|\Gamma|_{avg} \sim 0.31$ and the phase range is $\sim 321^\circ$, which follows the trend already observed in Figs. 3 and 5, *i.e.*, reducing the gap size produces a higher magnitude of reflection coefficient and a lower phase range. At $\lambda_c^{(2)}$, we have the secondary resonance with field enhancement at the extremities of the dipole nanoantenna. The average magnitude of reflection coefficient is lower (~ 0.2), as is the phase range ($\sim 244^\circ$). The lower phase range is due to the fact λ_{ENZ} crosses $\lambda_c^{(2)}$ at higher voltages than it does for λ_c such that the phase shifting mechanism described in subsection 2.3 is not fully exploited. We would need to further increase V_g (*i.e.*, N_{pert}) to extend the phase range.

2.6 Electrostatic simulations

In this subsection, we use electrostatic modelling to justify the choice of the perturbation parameters N_{pert} and t_{pert} used to simulate in the previous subsections the optical response of our pixels due to voltage biasing. We first consider a 1D cross-sectional model of our MOS capacitor, and then we present a 2D model which takes into account corner configurations which can be found in nanostructures.

2.6.1 Simulation details

The electrostatic modelling was conducted using Lumerical DEVICE, which solves the Poisson and drift-diffusion equations self-consistently [43]. We assume a work function for gold of $\phi_m = 5.1$ eV. For the oxide, we consider HfO₂, which is a high dielectric constant material of static relative permittivity $\epsilon_{DC}^{(HfO_2)} = 25$ [44,45]. ITO is treated as an n-doped semiconductor with $\epsilon_{DC}^{(ITO)} = 9.3$, electron affinity $\chi_s = 4.8$ eV, band gap energy $E_g = 2.8$ eV, effective mass of electrons as in optical simulation ($m_n^* = 0.35 \cdot m_e$), and effective mass of holes $m_p^* = m_e$ [32]. Since E_g is large, the intrinsic carrier concentration n_i is very small. We assume an unperturbed carrier (electron) density in ITO of $N_0 = 3 \cdot 10^{20}$ cm⁻³ [32], which corresponds to a Fermi energy located within the conduction band, so that ITO behaves as a degenerate semiconductor. We consider ITO at a potential of $V_s = 0$ V (grounded) and we apply a gate voltage V_g to the metal as depicted in Fig. 9(a).

Breakdown fields for oxides used in MOS systems depend strongly on the deposition process. Assuming a breakdown field for HfO₂ of $E_{bk} = 6.4$ MV/cm [27], for a nominal thickness of $t_{ox} = 5$ nm, we obtain a breakdown voltage of $V_{bk} = 3.2$ V. The parameters of HfO₂ are similar to those of HAOL, *i.e.*, a nanolaminate comprised of layers of Al₂O₃ and HfO₂ ($\epsilon_{DC}^{(HAOL)} = 22$ and $E_{bk} = 7.2$ MV/cm [32]), which could also be used in our phase shifting pixel as the insulating layer.

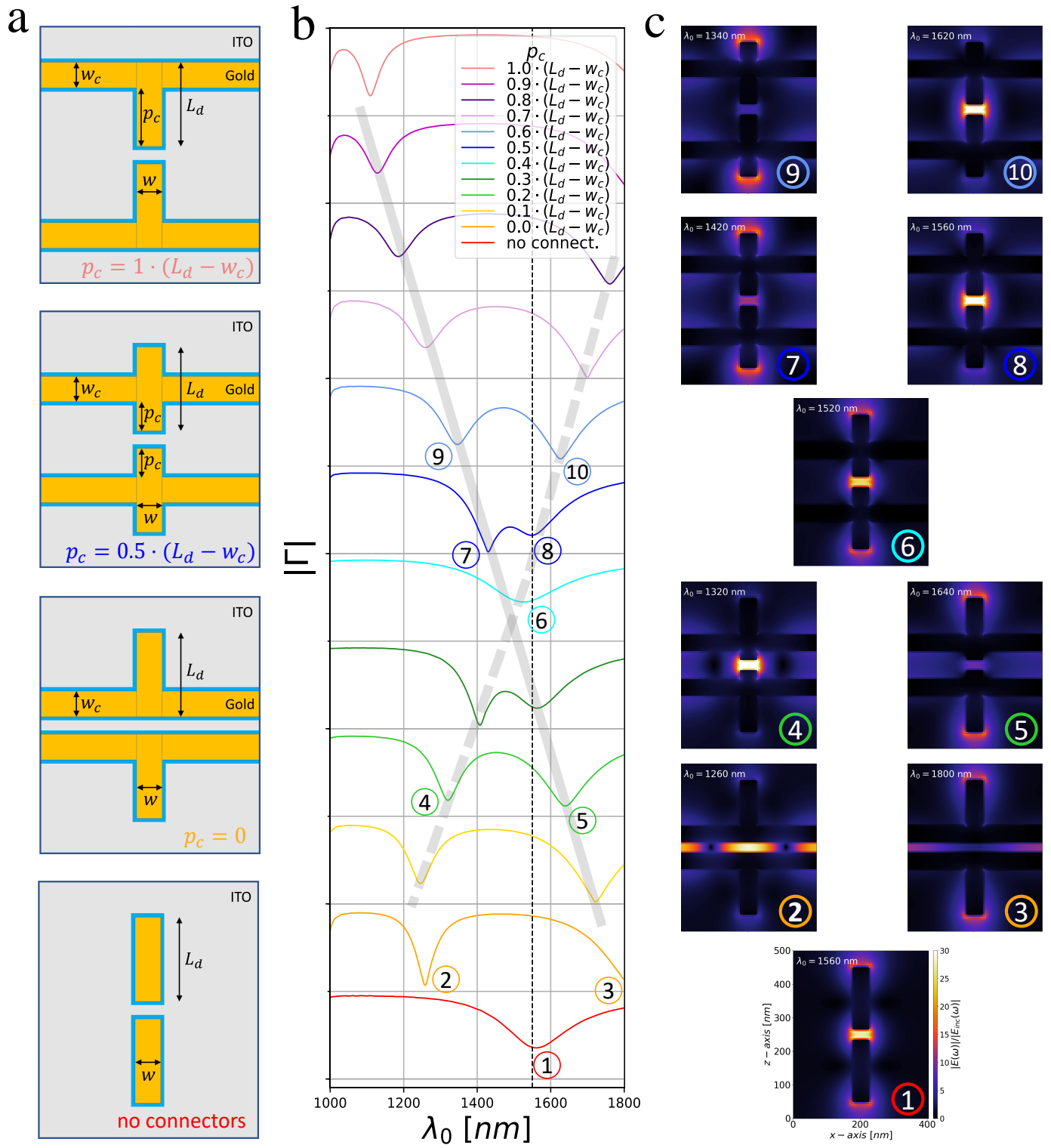


Figure 7: Effect of the connector position: (a) illustration of different connector configurations, (b) reflection coefficient for varying connector positions as sketched in Fig. 7(a), (c) field distribution for some resonances highlighted in Fig. 7(b).

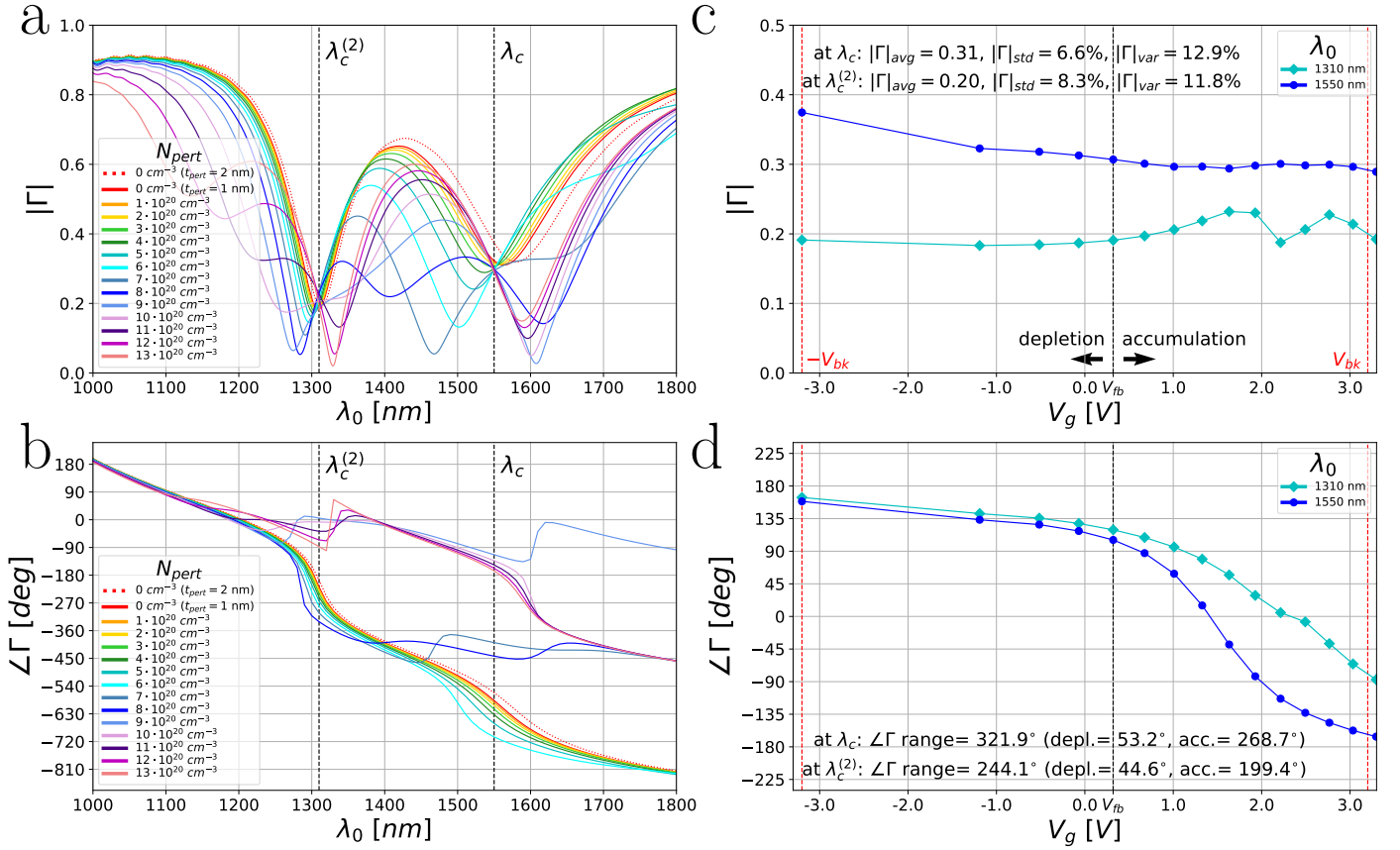


Figure 8: Fourth optimized pixel with parameters with $g = 20 \text{ nm}$, $L_d = 168 \text{ nm}$, $a_x = 348 \text{ nm}$, $t_m = 100 \text{ nm}$, and $p_c = 0.5 \cdot (L_d - w_c)$: (a) $|\Gamma|$ and (b) $\angle\Gamma$ vs λ_0 for varying N_{pert} within the t_{pert} layer. (c) $|\Gamma|$ and (d) $\angle\Gamma$ vs V_g for λ_0 near λ_c . The phase plots are unwrapped for clarity.

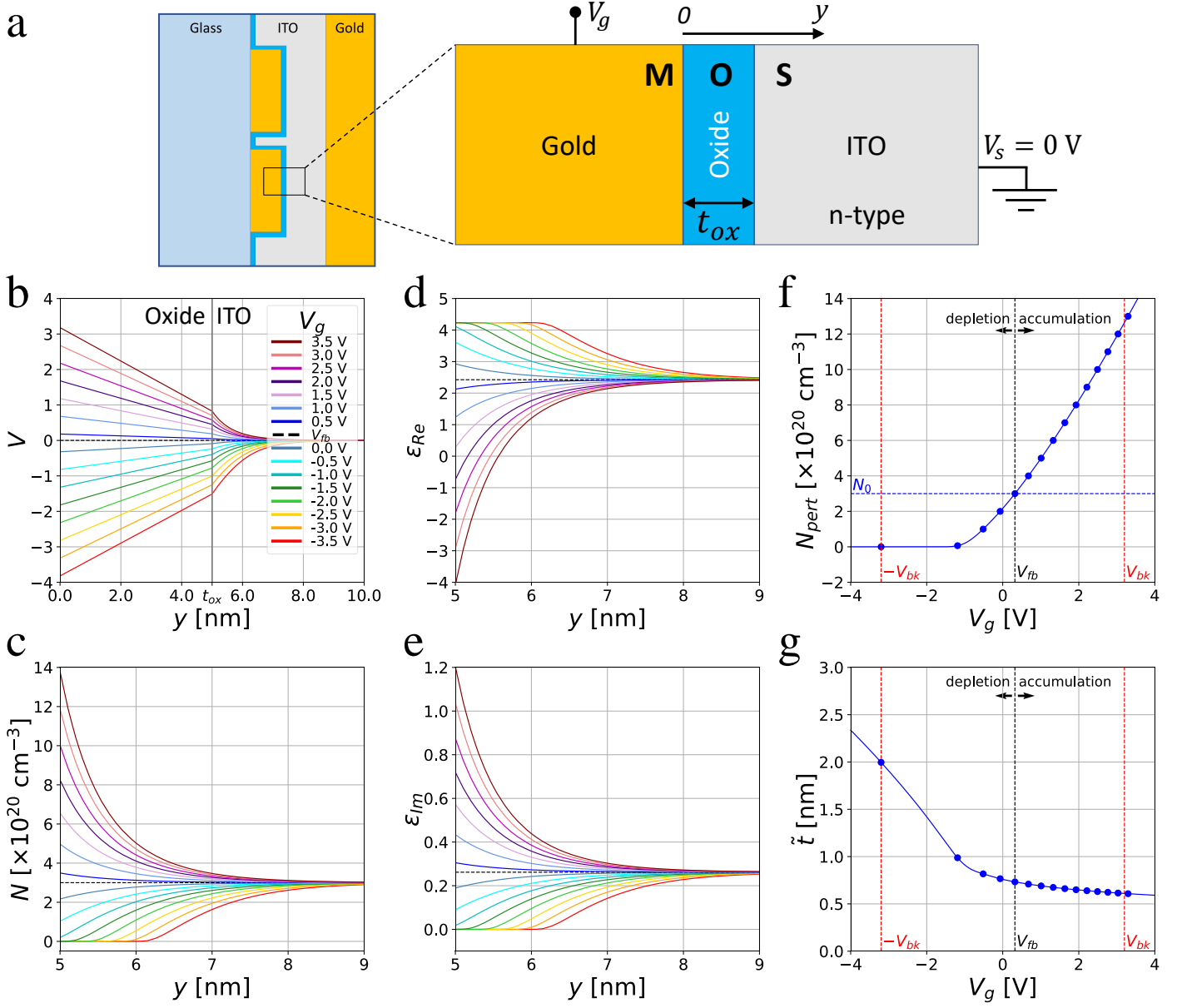


Figure 9: (a) Side view of the plasmonic pixel and zoom of the MOS 1D cross-section modelled. (b) Voltage across the oxide and ITO for varying V_g . (c) Carrier density across ITO for varying V_g . (d, e) ϵ_{Re} and ϵ_{Im} across ITO at λ_c for varying V_g . (f) N_{pert} as a function of V_g . (g) Effective perturbed ITO thickness \tilde{t} as a function of V_g . Figs. 9(b)–(e) share the same legend.

2.6.2 1D cross-section model

In Fig. 9(b), we show the potential V across the structure (oxide+ITO) for varying V_g , which reveals a flat band voltage $V_{fb} = 0.32$ V (value of V_g at which $V(y) = 0$). This means that for $V_g > V_{fb}$ the ITO layer goes into accumulation, whereas for $V_g < V_{fb}$ we have depletion.

From Fig. 9(c), we note that the carrier density in ITO increases with increasing gate voltage V_g . In order to maximize this carrier perturbation, we need to use an oxide with a high product of $\varepsilon_{DC} \cdot E_{bk}$. When no voltage is applied ($V_g = 0$ V), the MOS capacitor is slightly in depletion; we need to apply $V_g = V_{fb}$ in order to have an unperturbed carrier density across ITO, *i.e.*, $N_{pert} = N_0$ within the t_{pert} layer.

In Figs. 9(d) and 9(e), respectively, we show the complex permittivity ε_{Re} and ε_{Im} (at $\lambda_c = 1550$ nm, *i.e.*, the wavelength at which our pixels were optimized) by varying V_g and then N_{pert} within the perturbed ITO layer. We observe that for increasing V_g , ε_{Re} decreases becoming negative, and ε_{Im} increases, *i.e.*, the perturbed ITO layer becomes more and more metallic. Fig. 9(c) also shows that the perturbation of the carrier density is localized within a thickness of ~ 1 – 2 nm. In order to accurately resolve this perturbation, electrostatic computations were conducted with a discretization of ~ 0.05 nm, but this space step is challenging to apply in the corresponding 3D optical simulations, which are carried out here using a discretized space step of 1 nm. To model the perturbed carrier density in optical simulations, we need to homogenize the perturbation of the carrier density in ITO with respect to the unperturbed level N_0 . This is done by considering the $N(y)$ curves in Fig. 9(c), and by identifying a constant carrier density \tilde{N} and a constant thickness \tilde{t} such that

$$\tilde{N} \cdot \tilde{t} = \int_{t_{ox}}^{+\infty} (N(y) - N_0) dy. \quad (1)$$

We set $\tilde{N} = \lim_{y \rightarrow t_{ox}^+} N(y) - N_0$, that is, we use the limit value that $N(y)$ reaches at the boundary between the oxide and ITO. Finally, we retrieve $N_{pert} = \tilde{N} + N_0$, as plotted in Fig. 9(f) for varying V_g within the breakdown voltage range (identified by vertical red dashed lines). We note that N_{pert} varies between 0 (depletion regime) and $\sim 13 \cdot 10^{20}$ cm⁻³ (accumulation regime) as used in the optical simulations. Inverting Eq. (1), we derive \tilde{t} , which is shown in Fig. 9(g) as a function of V_g . In accumulation, we obtain a nearly constant \tilde{t} slightly lower than 1 nm, that we approximate with a perturbed ITO layer $t_{pert} = 1$ nm in the optical simulations. In depletion, the value of \tilde{t} increases up to ~ 2 nm with decreasing V_g . The case of full depletion with $t_{pert} = 2$ nm was exploited in the optical simulations to further extend the phase range of the pixel. The blue dots in Figs. 9(f) and 9(g) correspond to the blue dots in the optical simulation results for the four optimized pixels reported in Figs. 3, 5, 6, and 8.

As the $t_{pert} = 1$ nm approximation in the accumulation regime may overestimate the pixel performance, we performed optical simulations where the thickness of the perturbed layer was taken to be $t_{pert} = 0.5$ nm, and the simulation domain was discretized with a space step of 0.5 nm. In this case, by optimizing the pixel to find a constant amplitude point at λ_c , we obtained a lower magnitude of the reflection coefficient and an increased phase range, following the trade-off between phase range and amplitude. This result suggests that the phase range of the reflection coefficient at λ_c depends on the range of N_{pert} , while its amplitude depends on the thickness t_{pert} of the perturbed ITO layer.

2.6.3 2D correction to 1D model

The MOS structure analyzed in 1D in Fig. 9 does not take into account the geometry of a nanoantenna. Since our plasmonic pixel (Fig. 1) is more complex as corners are involved, we performed a MOS study for a 2D geometry containing four different corner types as shown in Fig 10. In quadrant 1 (top right), we consider a rounded metal corner of radius $r_1^M = 5$ nm and a rounded oxide corner of radius $r_1^O = r_1^M + t_{ox} = 10$ nm. In quadrant 2 (top left), we have a square metal corner and a rounded oxide corner with $r_2^O = 5$ nm. In quadrant 3 (bottom left), both metal and oxide corners are square. In quadrant 4, both metal and oxide corners are rounded and of the same radius $r_4^M = r_4^O = 5$ nm. Figs. 10(a), 10(b) and 10(c) show, respectively, the potential distribution $V(x, z)$, the electric field distribution $|E(x, z)|$ and the carrier density distribution $N(x, z)$ for $V_g = 1$ V and ITO grounded ($V_s = 0$ V). We observe that V , E , and N exhibit a different behaviour at the corners compared to regions away from the corners where the behaviour of the 1D system is recovered. As the corner becomes more rounded (quadrant 1 in Fig. 10(c)), the carrier density N approaches that calculated for the 1D system. These results suggest that the perturbed layer in ITO should be modelled by a variable thickness depending on the roundness of the corners. However, the results of optical simulations of a nanoantenna with corners as in quadrant 1 (not shown), reproduce the physical operation of pixels containing all square corners with uniform t_{pert} ; thus, for ease of simulation, square corners and uniform t_{pert} only are used throughout this paper. To consider round corners, the pixels as presented here would need to be re-optimized, as round corners produce a blue shift in the optical response due to the smaller total volume of rounded nanostructures versus square ones, all other geometrical parameters being equal.

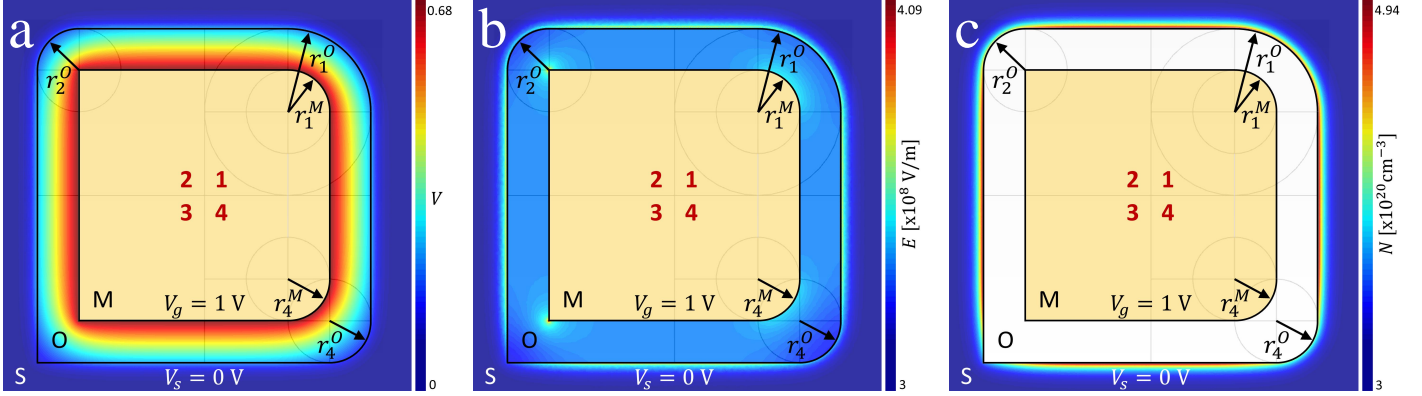


Figure 10: (a) Potential, (b) electric field, and (c) carrier density distributions from electrostatic simulation of a representative MOS structure with four types of rounded corners for $V_g = 1$ V.

3 Simulation of phased arrays for 1D beam steering

In Section 2, we designed our pixels such that the pitch is small enough to avoid grating lobes due to the pitch size ($a_z, a_x < \lambda/2$) for any steering angle, yet large enough to avoid coupling between adjacent pixels due to near-field interaction. In order to validate our pixel designs for beam steering, we numerically test one of them (third optimized pixel in Fig. 6) in an array configuration. While in Section 2 we optimized the response of our pixels by applying periodic boundary conditions, which is equivalent to simulating an infinite array of pixels under the same perturbation, here, we create an array of pixels in the xz -plane, as sketched in Fig. 11(a). The arrangement of connectors makes the system controllable row by row, which means that all nanoantennas in the same row will share the same potential, and thus the same phase of the reflection coefficient. By varying the phase associated with the pixels along z , we produce beam steering in the yz -plane ($\phi_s = 0$) with a steering angle θ_s ; in our example there is no steering in the xy -plane.

We cannot simulate arbitrarily large arrays with our FDTD model, so we apply periodic boundary conditions on an extended unit cell containing one pixel along x and M_z pixels along z . Thus, along z , each pixel produces a different phase of the reflection coefficient $\psi(q)$, with the position of the pixels in z labelled by $q = 1, \dots, M_z$. To enforce a phase gradient along z in the array, which is necessary for beam steering, we need a constant phase difference between adjacent pixels along z , $\Delta\psi_z = \psi(q+1) - \psi(q)$. This sets a condition on $\Delta\psi_z$ in our simulations, which can only assume the values $|\Delta\psi_z| = 2\pi/M_z$. Knowing $\Delta\psi_z$, the steering angle θ_s can be analytically determined via the generalized form of Snell's law of reflection [46]:

$$k \sin \theta_s = \frac{\Delta\psi_z}{a_z} + k \sin \theta_i, \quad (2)$$

where $k = 2\pi n_{\text{SiO}_2}/\lambda_c$, θ_i is the angle of incidence (in our case, we have normal incidence, *i.e.*, $\theta_i = 0$) and θ_s is the angle of the reflected/steered beam.

We consider an extended unit cell with $M_z = 8$ and $\Delta\psi_z = -45^\circ$. Using the curve for $\lambda_c = 1550$ nm in Fig. 6(d), we determine the voltage that must be applied to each row to produce the required phase of the reflection coefficient $\psi(q)$ for each nanoantenna in the extended unit cell. Note that applying a voltage in an optical simulation corresponds to using a specific value of N_{pert} derived via the relation between V_g and N_{pert} in Fig. 9(f). The array is excited by a monochromatic plane wave at λ_c which is z -polarized and normally incident on the metasurface. The reflected field is obtained by subtracting the incident field from the total field. In Fig. 11(b), we plot the phase of the reflected field E_z , from which we note that the phase front of the reflected wave is flat and propagates at an angle of $\theta_s = -15.5^\circ$ with respect to the normal to the plane of the array, as confirmed by Eq. (2). We find that the amplitude of the reflected field E_z is nearly uniform with a percentage variation $|E_z|_{\text{var}} = 5.6\%$. These phase and amplitude profiles indicate beam steering.

The flat phase front reflected from the array only provides qualitative information about the steering. To further validate the beam steering, the radiation pattern in the far-field must be observed. From the near-fields in the reflection region, we calculate the far-fields via a near-to-far-field transformation [39], and then obtain the radiation pattern by squaring the far-fields. This near-to-far-field transformation is carried out considering $P_z = 25$ periods of the extended unit cell such to mimic an array with 200 pixels. The radiation pattern allows us to quantify how the electromagnetic power is distributed in space as a function of angle, and thus, to quantify the quality of the beam steering in terms of intensity of the long-period grating lobes. In Fig. 11(c), we show the normalized radiation pattern $|U(\theta_s, \phi_s)|^2$ in the yz -plane ($\phi_s = 0^\circ$). In the top panel we show the contour plot of the far-field reflected power as a function of wavelength (varying from $\lambda_0 = 1500$ nm to 1600 nm) and far-field angle θ_s . The contour plot reveals that near λ_c the specular reflection in the normal direction disappears (black region in the colour band for $\theta_s = 0^\circ$). Looking at this black region, we calculate the wavelength range such that the far-field intensity in the normal direction is two orders of magnitude lower

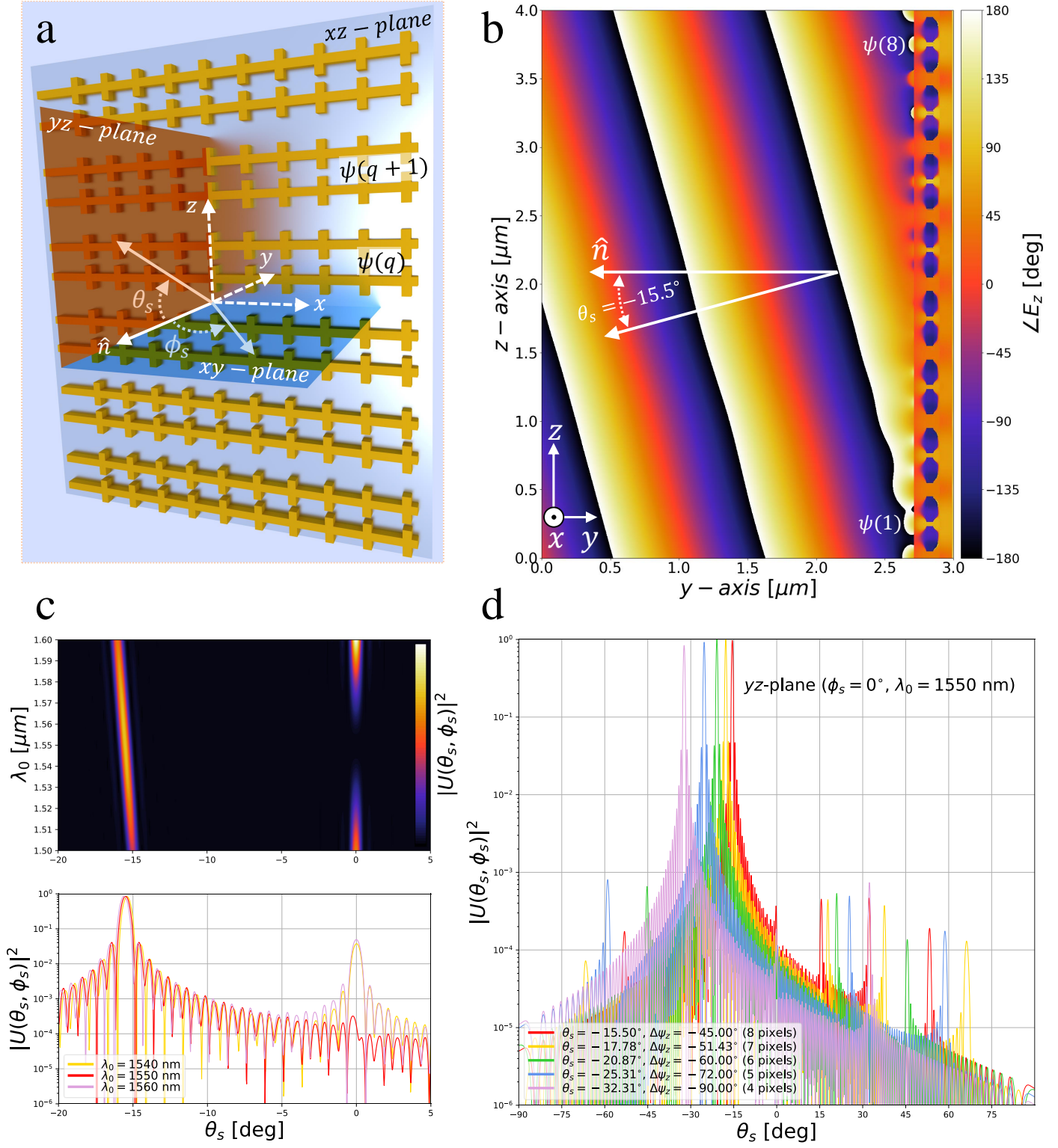


Figure 11: (a) Sketch of an array of pixels with coordinates, (b) $\angle E_z$ and (c) radiation pattern in the yz -plane ($\phi_s = 0^\circ$) for an extended unit cell ($M_z = 8$, $\theta_s = -15.5^\circ$), (d) radiation pattern for extended unit cells with $M_z = 4, 5, 6, 7, 8$ pixels.

than the main beam, corresponding to a beam steering bandwidth of ~ 10 nm. The bottom panel contains three curves extracted from the contour plot on a log scale, where we see that for $\lambda_c = 1550$ nm the long-period grating lobe at $\theta_s = 0^\circ$ is more than two orders of magnitude less intense than for $\lambda_0 = 1540$ and 1560 nm. These results validate the optimization at λ_c of the single pixel, as they show that at λ_c the specular reflection is negligible and the beam is completely steered.

In Fig. 11(d), we show the radiation patterns for different values of $M_z = \{4, 5, 6, 7, 8\}$, calculated via near-to-far-field transformation using $P_z = \{50, 40, 34, 29, 25\}$, respectively, such that $M_z \cdot P_z \sim 200$. These M_z values correspond to decreasing values of $\Delta\psi_z$ and thus steering angle θ_s , as reported in the legend of Fig. 11(d). From phased antenna array theory, we know that the radiation pattern of the array is obtained by multiplying the radiation pattern of the single emitter F with an array factor A that depends on the arrangement of the emitters, *i.e.*, $|U(\theta_s, \phi_s)|^2 = |F(\theta_s, \phi_s)|^2 |A(\theta_s, \phi_s)|^2$. As $A(\theta_s, \phi_s)$ reaches the same maximum value for any steering angle, the fact that the peak of the radiation patterns in Fig. 11(d) decreases with increasing steering angle suggests that each nanoantenna exhibits a dipole-like radiation pattern in reflectance. All the radiation patterns show long-period grating lobes which are more than three orders of magnitude lower than the main lobe, confirming beam steering over a wide angular range. We note that this array simulation approach does not take into account the limited phase range of the pixel, as M_z is chosen such that $(M_z - 1)|\Delta\psi_z|$ is lower than the phase range of the pixel. The long-period grating lobes that we observe are only due to the non-uniform amplitude of the reflection coefficient as V_g varies, and they obey the diffraction grating equation:

$$\sin \theta_s^{(m)} = m\lambda / (a_z M_z), \quad (3)$$

where $a_z M_z$ is the size of the extended unit cell (our long period), and m is the diffraction order ($m = 1$ identifies the main lobe). Movies 1 and 2 (Supporting Information) show the time-domain evolution of the absolute value of the electric field for $M_z = 8$ ($\Delta\psi_z = -45^\circ$, $\theta_s = -15.5^\circ$) and $M_z = 4$ ($\Delta\psi_z = -90^\circ$, $\theta_s = -32.31^\circ$). The scattered-field region contains only the steered beam and is thus made large in the simulation for visual clarity, while the total-field region contains both the reflected and incident fields, and is thus limited to the vicinity of the metasurface where the input signal is injected. As this is a time-domain simulation, we find that the steering does not occur instantaneously, as the phase relations responsible for the creation of the steered beam take some time to build up.

4 Conclusion

We propose a novel plasmonic pixel for beam steering applications in reflectarray configurations. The pixel is of sub-wavelength dimensions, and exhibits a reflection coefficient that, at a specific operating wavelength, varies with applied voltage over a large phase range with nearly constant amplitude. The structure consists of a plasmonic dipole nanoantenna on a substrate covered conformally by a thin oxide layer and ITO. Electrically, the structure forms a MOS capacitor with the nanoantenna acting as the electrical contact of the capacitor. The MOS capacitor is exploited to perturb the free electron density within a region of ITO in contact with the oxide. This perturbed layer of ITO will experience a change of its epsilon-near-zero wavelength as a function of applied voltage, eventually crossing the resonance wavelength of the nanoantenna. When this occurs, the environment surrounding the nanoantenna switches from all dielectric to one containing a metallic shell. This abruptly changes the resonance of the nanoantenna and causes a large phase shift in its reflection coefficient.

We found that the phase range of the reflection coefficient depends on the maximum carrier density perturbation induced in ITO which is bounded by the oxide breakdown voltage. Moreover, the magnitude of the reflection coefficient at the operating wavelength depends on the thickness of this perturbation, but can be made uniform across the phase range by optimizing the geometrical parameters. We analyzed the performance of several pixel designs and found that a phase range of 330° is possible with a nearly flat magnitude of the reflection coefficient of 0.2; higher magnitudes of ~ 0.4 are possible if we can accept a phase range of 300° .

We also found that there is an optimal position for the electrical connectors where they contribute minimally to the optical response of the nanoantenna. However, in an alternate position, their effect may be exploited for realizing dual-band beam steering. Though the performance of the proposed pixel is primarily limited by the breakdown field of the oxide, the phase and amplitude responses of the reflection coefficient achieved with materials currently available are highly promising for beam steering applications, as demonstrated by our 3D optical simulations of beam steering in 1D.

Acknowledgments

We acknowledge computational support from Compute Canada, and financial support from NSERC and Huawei Technologies Canada.

References

- [1] Heck, M. J. Highly integrated optical phased arrays: Photonic integrated circuits for optical beam shaping and beam steering. *Nanophotonics* (2017).
- [2] Meinzer, N., Barnes, W. L. & Hooper, I. R. Plasmonic meta-atoms and metasurfaces. *Nature Photonics* **8**, 889–898 (2014).
- [3] Genevet, P., Capasso, F., Aieta, F., Khorasaninejad, M. & Devlin, R. Recent advances in planar optics: from plasmonic to dielectric metasurfaces. *Optica* **4**, 139 (2017).
- [4] Scheuer, J. Metasurfaces-based holography and beam shaping: Engineering the phase profile of light. *Nanophotonics* (2017).
- [5] Chen, S., Li, Z., Zhang, Y., Cheng, H. & Tian, J. Phase manipulation of electromagnetic waves with metasurfaces and its applications in nanophotonics. *Advanced Optical Materials* **6**, 1800104 (2018).
- [6] Papaioannou, M., Plum, E., Rogers, E. T. & Zheludev, N. I. All-optical dynamic focusing of light via coherent absorption in a plasmonic metasurface. *Light: Science & Applications* **7**, 17157 (2018).
- [7] Chen, W. T. *et al.* A broadband achromatic metalens for focusing and imaging in the visible. *Nature Nanotechnology* **13**, 220–226 (2018).
- [8] Arroyo Huidobro, P., Maier, S. A. & Pendry, J. B. Tunable plasmonic metasurface for perfect absorption. *EPJ Applied Metamaterials* **4**, 6 (2017).
- [9] Lee, T., Jang, J., Jeong, H. & Rho, J. Plasmonic- and dielectric-based structural coloring: from fundamentals to practical applications. *Nano Convergence* **5**, 1 (2018).
- [10] Silva, A. *et al.* Performing Mathematical Operations with Metamaterials. *Science* **343**, 160–163 (2014).
- [11] Huang, L., Zhang, S. & Zentgraf, T. Metasurface holography: from fundamentals to applications. *Nanophotonics* **7**, 1169–1190 (2018).
- [12] Calà Lesina, A., Ramunno, L. & Berini, P. Dual-polarization plasmonic metasurface for nonlinear optics. *Optics Letters* **40**, 2874 (2015).
- [13] Yue, F. *et al.* Vector Vortex Beam Generation with a Single Plasmonic Metasurface. *ACS Photonics* **3**, 1558–1563 (2016).
- [14] Calà Lesina, A., Berini, P. & Ramunno, L. Vectorial control of nonlinear emission via chiral butterfly nanoantennas: generation of pure high order nonlinear vortex beams. *Optics Express* **25**, 2569 (2017).
- [15] Zeng, S. *et al.* Graphene-Gold Metasurface Architectures for Ultrasensitive Plasmonic Biosensing. *Advanced Materials* **27**, 6163–6169 (2015).
- [16] Jiang, N., Zhuo, X. & Wang, J. Active Plasmonics: Principles, Structures, and Applications. *Chemical Reviews* **118**, 3054–3099 (2018).
- [17] Kang, L., Jenkins, R. P. & Werner, D. H. Recent progress in active optical metasurfaces. *Advanced Optical Materials* **7**, 1801813 (2019).
- [18] Shaltout, A. M., Shalaev, V. M. & Brongersma, M. L. Spatiotemporal light control with active metasurfaces. *Science* **364**, eaat3100 (2019).
- [19] Li, J. *et al.* Addressable metasurfaces for dynamic holography and optical information encryption. *Science Advances* **4**, eaar6768 (2018).
- [20] Zhang, L. *et al.* Space-time-coding digital metasurfaces. *Nature Communications* **9**, 4334 (2018).
- [21] Yin, X. *et al.* Active Chiral Plasmonics. *Nano Letters* **15**, 4255–4260 (2015).
- [22] Duan, X., Kamin, S. & Liu, N. Dynamic plasmonic colour display. *Nature Communications* **8**, 14606 (2017).
- [23] Ratni, B., de Lustrac, A., Piau, G.-P. & Burokur, S. N. Electronic control of linear-to-circular polarization conversion using a reconfigurable metasurface. *Applied Physics Letters* **111**, 214101 (2017).

- [24] Wang, Z. *et al.* Metasurface-based focus-tunable mirror. *Opt. Express* **27**, 30332–30339 (2019).
- [25] Busschaert, S. *et al.* Beam steering with a nonlinear optical phased array antenna. *Nano Letters* **19**, 6097–6103 (2019).
- [26] Forouzmand, A., Salary, M. M., Inampudi, S. & Mosallaei, H. A Tunable Multigate Indium-Tin-Oxide-Assisted All-Dielectric Metasurface. *Advanced Optical Materials* **6**, 1701275 (2018).
- [27] Olivieri, A. *et al.* Plasmonic Nanostructured Metal-Oxide-Semiconductor Reflection Modulators. *Nano Letters* (2015).
- [28] Zhu, Z., Evans, P. G., Haglund, R. F. & Valentine, J. G. Dynamically Reconfigurable Metadevice Employing Nanostructured Phase-Change Materials. *Nano Letters* (2017).
- [29] Komar, A. *et al.* Dynamic Beam Switching by Liquid Crystal Tunable Dielectric Metasurfaces. *ACS Photonics* (2018).
- [30] Sherrott, M. C. *et al.* Experimental Demonstration of >230 Phase Modulation in Gate-Tunable Graphene-Gold Reconfigurable Mid-Infrared Metasurfaces. *Nano Letters* **17**, 3027–3034 (2017).
- [31] Huang, Y.-W. *et al.* Gate-Tunable Conducting Oxide Metasurfaces. *Nano Letters* **16**, 5319–5325 (2016).
- [32] Kafaie Shirmanesh, G., Sokhoyan, R., Pala, R. A. & Atwater, H. A. Dual-Gated Active Metasurface at 1550 nm with Wide (>300) Phase Tunability. *Nano Letters* **18**, 2957–2963 (2018).
- [33] Sun, J., Timurdogan, E., Yaacobi, A., Hosseini, E. S. & Watts, M. R. Large-scale nanophotonic phased array. *Nature* (2013).
- [34] Xun, M. *et al.* Phase tuning in two-dimensional coherently coupled vertical-cavity surface-emitting laser array. *Appl. Opt.* **55**, 5439–5443 (2016).
- [35] Lee, J. *et al.* Ultrafast Electrically Tunable Polaritonic Metasurfaces. *Advanced Optical Materials* (2014).
- [36] Feigenbaum, E., Diest, K. & Atwater, H. A. Unity-order index change in transparent conducting oxides at visible frequencies. *Nano Letters* (2010).
- [37] Lee, H. W. *et al.* Nanoscale conducting oxide PlasMOSStor. *Nano Letters* (2014).
- [38] Forouzmand, A. & Mosallaei, H. Real-Time Controllable and Multifunctional Metasurfaces Utilizing Indium Tin Oxide Materials: A Phased Array Perspective. *IEEE Transactions on Nanotechnology* **16**, 296–306 (2017).
- [39] Taflove, A. & Hagness, S. C. *Computational Electrodynamics: The Finite-Difference Time-Domain Method, Third Edition* (2005).
- [40] Calà Lesina, A., Vaccari, A., Berini, P. & Ramunno, L. On the convergence and accuracy of the FDTD method for nanoplasmonics. *Optics Express* **23**, 10481 (2015).
- [41] McPeak, K. M. *et al.* Plasmonic Films Can Easily Be Better: Rules and Recipes. *ACS Photonics* **2**, 326–333 (2015).
- [42] Wood, D. L., Nassau, K., Kometani, T. Y. & Nash, D. L. Optical properties of cubic hafnia stabilized with yttria. *Applied Optics* **29**, 604 (1990).
- [43] URL <https://www.lumerical.com/>.
- [44] Wilk, G. D., Wallace, R. M. & Anthony, J. M. High- κ gate dielectrics: Current status and materials properties considerations. *Journal of Applied Physics* (2001).
- [45] Robertson, J. High dielectric constant gate oxides for metal oxide Si transistors. *Reports on Progress in Physics* (2006).
- [46] Yu, N. *et al.* Light propagation with phase discontinuities: Generalized laws of reflection and refraction. *Science* (2011).